



OPEN

Structure-controlled asperities of the 1920 Haiyuan *M*8.5 and 1927 Gulang *M*8 earthquakes, NE Tibet, China, revealed by high-resolution seismic tomography

Quan Sun^{1,2}, Shunping Pei^{1,2,3}✉, Zhongxiong Cui⁴, Yongshun John Chen⁵, Yanbing Liu^{1,2}, Xiaotian Xue^{1,2}, Jiawei Li^{1,2}, Lei Li^{1,2} & Hong Zuo^{1,2}

Detailed crustal structure of large earthquake source regions is of great significance for understanding the earthquake generation mechanism. Numerous large earthquakes have occurred in the NE Tibetan Plateau, including the 1920 Haiyuan *M*8.5 and 1927 Gulang *M*8 earthquakes. In this paper, we obtained a high-resolution three-dimensional crustal velocity model around the source regions of these two large earthquakes using an improved double-difference seismic tomography method. High-velocity anomalies encompassing the seismogenic faults are observed to extend to depths of 15 km, suggesting the asperity (high-velocity area) plays an important role in the preparation process of large earthquakes. Asperities are strong in mechanical strength and could accumulate tectonic stress more easily in long frictional locking periods, large earthquakes are therefore prone to generate in these areas. If the close relationship between the asperity and high-velocity bodies is valid for most of the large earthquakes, it can be used to predict potential large earthquakes and estimate the seismogenic capability of faults in light of structure studies.

Earthquakes occur when the stored energy in the Earth's lithosphere is suddenly released. Large earthquakes usually cause great hazards on natural environment and/or humans. There has been an obvious surge of great earthquakes with magnitudes ≥ 8.0 during the past decade with great diversity at various aspects¹. The diversity of earthquake source is generally associated with the geometrical complexities of the fault systems, which are attributed to the heterogeneity of the dynamic rupture process²⁻⁵. Moreover, earthquake processes are significantly affected by the heterogeneity of mechanical properties of the fault zone, often represented conceptually as asperities⁶⁻⁸. Faults that are fully or partially locked by strong asperities breed great seismic hazard because the accumulated stress on the asperities are prone to be released through large earthquakes, contrasting sharply with the faults which are characterized by creeping deformation⁹⁻¹¹. Seismological studies suggest the occurrence of strong earthquakes is closely related to the abnormal distribution of crustal velocity¹²⁻¹⁵. Therefore, studying the fine velocity structure around the source regions could shed light on the relationship between the velocity features and large earthquakes and furtherly the seismogenic mechanism of large earthquakes.

Various studies have been conducted to explore the crustal structure of the large earthquake source regions and link the observations to mechanism of earthquake generation¹⁶⁻¹⁸. Besides, there have been a growing number of observations and numerical simulation studies on asperity^{7,19-22}. However, so far there are few studies on the high-resolution local crustal structure surrounding the source regions of large earthquakes. To investigate the effects of structural heterogeneity on large earthquake generation, we explored the body-wave crustal velocity structure in the NE Tibetan Plateau where is high on seismicity (Fig. 1) and is therefore an ideal natural laboratory to study the seismogenic mechanism of large earthquakes. As one of the most active areas in continental

¹Key Laboratory of Continental Collision and Plateau Uplift, Institute of Tibetan Plateau Research, Chinese Academy of Sciences (CAS), Beijing 100101, China. ²University of Chinese Academy of Sciences, Beijing 100049, China. ³CAS Center for Excellence in Tibetan Plateau Earth Sciences, Chinese Academy of Sciences (CAS), Beijing 100101, China. ⁴Department of Earth and Environmental Sciences, Lehigh University, Bethlehem, PA 18015, USA. ⁵Department of Ocean Science and Engineering, Southern University of Science and Technology, Shenzhen 518055, China. ✉email: peisp@itpcas.ac.cn

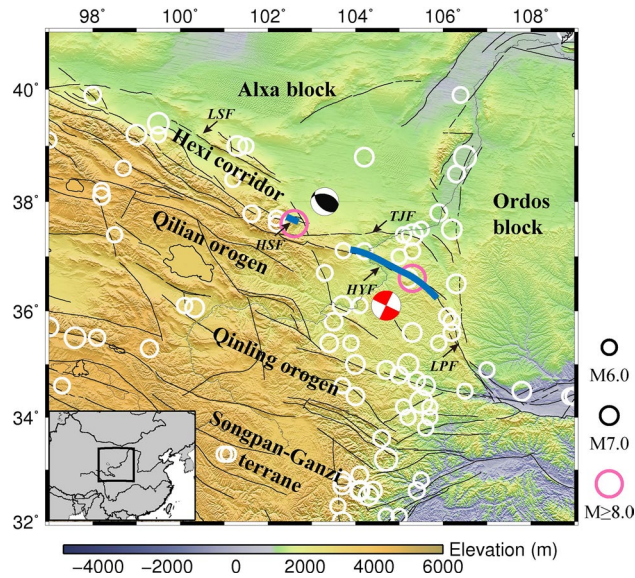


Figure 1. Tectonic background of the NE Tibetan Plateau and its surrounding areas. The white circles denote the locations of earthquakes larger than magnitude 6.0 and their sizes are proportional to magnitude. The two pink circles represent the 1920 Haiyuan $M8.5$ earthquake (on the right) and 1927 Gulang $M8$ earthquake (on the left), respectively. The two thick blue lines show the rough surface rupture zones of these two large earthquakes^{23,24}, while their focal mechanisms are displayed by the two nearby beach balls respectively^{23,25}. The black thin lines illustrate the main active faults²⁶, among which the major ones are abbreviated as followings: LSF, Longshoushan fault; HSF, Huangcheng-Shuangta fault; TJF, Tianjingshan fault; HYF, Haiyuan fault; LPF, Liupanshan fault. The maps are created using Generic Mapping Tools (GMT)²⁷ (v.4.2.1, <https://www.generic-mapping-tools.org/>).

China, numerous large earthquakes occurred there, including the 1920 Haiyuan $M8.5$ earthquake and 1927 Gulang $M8$ earthquake. These two earthquakes are extremely destructive and have led to a heavy loss on life and property. Though nearly 100 years have passed since the Haiyuan earthquake, there has not been enough research on these two large events due to the lack of data. Fortunately, in recent decades, abundant seismic data are increasingly available in the NE Tibetan Plateau, enabling us to obtain its high-resolution velocity structure and explore the seismogenic mechanism of the associated large earthquakes.

In this work, we improved the double-difference seismic tomography method and applied it to obtain a high-resolution three-dimensional (3-D) P wave and S wave velocities (V_p and V_s) model around the focal regions of the 1920 Haiyuan $M8.5$ and 1927 Gulang $M8$ earthquakes. Through analyzing their velocity features, we investigated the relationship between large earthquakes and velocity structure. Furthermore, we explored the seismogenic mechanism of large earthquakes in light of the asperity (high- V patches) which provides a guide for further seismic hazard assessment and associated disaster reduction. The detailed geometrical shape of fault plane is usually tough to depict, we therefore mainly discuss the seismogenic mechanism in terms of the structure features of the surrounding rocks.

Data

Sufficient observed seismic data and additional picking of later phases are critical for high-resolution tomography. In this work, we collected large amount of travel time data in the study region from two sources: the history data from Gansu, Ningxia, Inner Mongolia and Qinghai provinces (1985–2008) and uniform data from National Earthquake Data Center (2009–2018) (<http://data.earthquake.cn/>)²⁸. We carried out the following criteria on data selection: (1) all of the seismic hypocenters and seismic stations are distributed in the range of 32° – 41° N latitude and 97° – 109° E longitude. (2) Each event was recorded at least by 5 stations. (3) The epicentral distances for Pn and Sn waves are larger than 2° ²⁹. (4) The travel time residuals are less than 5.0 s. We finally obtained 325,829 Pg wave, 27,903 Pn wave, 311,646 Sg wave and 8,783 Sn wave from 34,997 local earthquakes recorded by 124 permanent and temporary seismic stations (Figure S1). The selected travel times of Pg, Pn, Sg and Sn wave exhibit universally linear relationship with the epicentral distance (Fig. 2).

Results

Resolution tests. Checkerboard test is a routine process for assessing the resolution and reliability of tomographic images. We assigned alternatively positive and negative velocity perturbations of 5% to the adjacent inversion grids of the initial velocity model. The synthetic travel times were calculated using the same ray distribution as the real data. Subsequently we applied our improved tomoDD method to obtain the recovered images and then compared with the original checkerboard model to check the recovery degree. Figure S3a and S3b shows the recovered checkerboard patterns for V_p and V_s tomographies around the source regions of Haiyuan

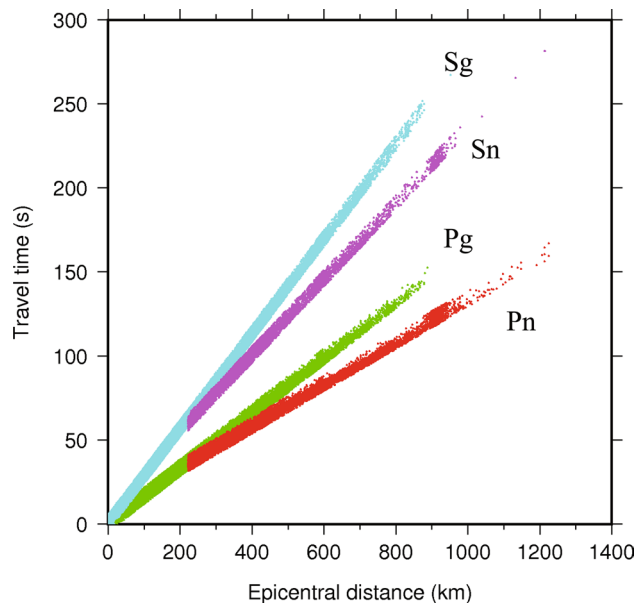


Figure 2. The distribution of travel times versus epicentral distance. The four different seismic phases are shown by different colors, with Sg (cyan), Sn (magenta), Pg (green) and Pn (red) from top to bottom.

and Gulang earthquakes with the lateral grid interval of 0.2° , respectively. On the whole, the checkerboard patterns were well recovered with resolution reaching to 0.2° above 15 km. Synthetic tests were also carried out to assess the reliability of the velocity anomalies, and these tests demonstrate that the main features of our tomographic results are well recovered at most of the areas (Figure S4 and S5).

The velocity structure around the 1920 Haiyuan earthquake. The 1920 Haiyuan $M8.5$ earthquake is one of the largest seismic events in continental China with an estimated hypocenter of longitude 105.3°E , latitude 36.6°N and depth 11 km³⁰. It occurred on the Haiyuan fault, which is a sinistral strike-slip fault zone with a length span of ~ 1000 km and it connects the Qilian orogen to the west and the Qinling orogen to the east³¹. The fault rupture of this event is suggested to be about 220 km long³². Intraplate earthquakes in general occur within the brittle upper crust above 15 km. Figure 3a,b and 4c,d show the inverted velocity perturbations of P and S wave at different layers relative to the average velocity at each depth, respectively. The patterns of V_p and V_s images are generally similar to each other, although the size and amplitude of anomalies are slightly different somewhere which might be attributed to the relatively lower resolution of V_s maps. At the depth of 5 km, Haiyuan earthquake source region is dominated by southeastward elongated high- V anomalies surrounded by low- V anomalies, although the low- V anomalies in the V_s map are not as clear as that of V_p structure at the southwest of the source region. The high- V anomalies in Haiyuan earthquake source region extend downwards to the depth of 10 km, and are even visible at 15 km at V_p results but shrink in size and amplitude.

The tomographic velocity structure around the Haiyuan earthquake is comparable to the results from a more accurate deep seismic sounding study along longitude $\sim 105.5^\circ$, which observed high- V anomalies above 25 km crossing Haiyuan fault³⁰. The magnetotelluric study around the Haiyuan earthquake zone also demonstrated high resistivity in the focal area³³, which is consistent with our results.

The velocity structure around the 1927 Gulang earthquake. The $M8$ Gulang earthquake occurred on 23 May 1927 is another large event in the Haiyuan-Qilian fault belt after the 1920 Haiyuan earthquake. Its epicenter is approximately located at 37.6°N and 102.6°E ³⁴. The surface-rupture zone is however much shorter, only 23 km long along the thrust³⁵. From the high-resolution 3-D models obtained in this paper (Figs. 3a,b and 4a,b), Gulang earthquake source region has similar velocity patterns as Haiyuan earthquake and is dominated by high- V anomalies between 5 and 15 km. Especially on the V_s map, the high- V features are more obvious above 10 km. The focal area is surrounded by low- V anomalies, such as the Hexi corridor and southern area to the Gulang earthquake.

The significant high- V features which are noticeable above 15 km beneath the focal area of the Gulang earthquake have also been observed by a series of previous seismic tomography studies^{36,37}, but our results show the anomalies in a much higher resolution due to the improved method and abundant data. The magnetotelluric sounding results show similar patterns with high-resistivity features above the focal area³⁸. The gravity study also find high-density anomalies in the Gulang earthquake source region with high- V structures³⁹.

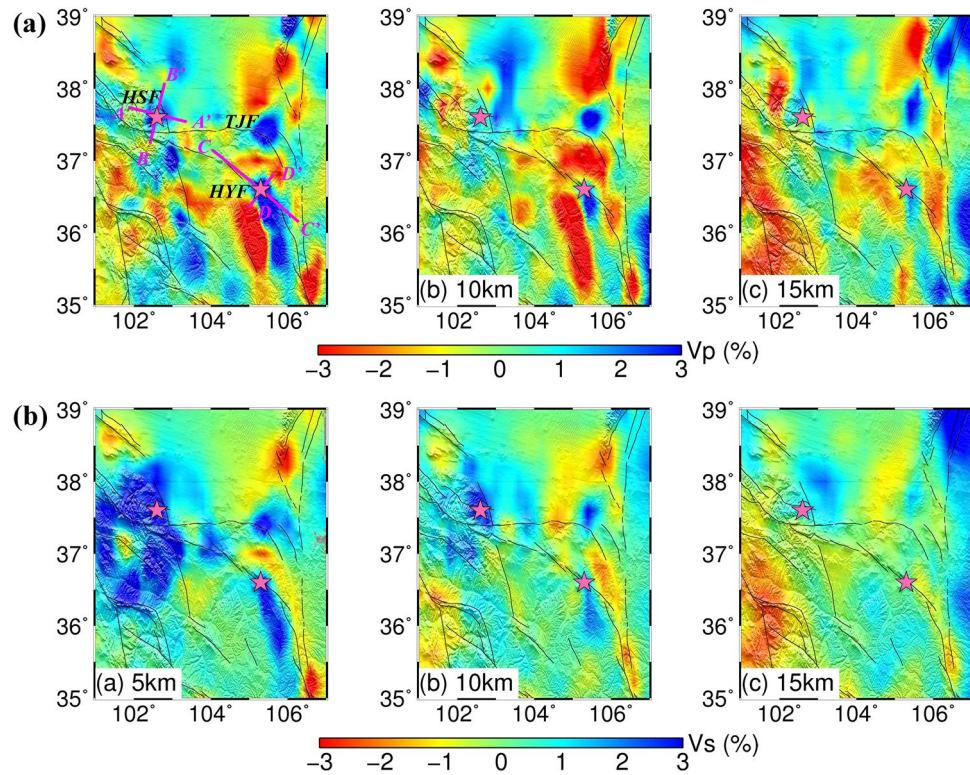


Figure 3. Tomographic Vp image (a) and Vs image (b) around the source regions of the 1920 Haiyuan and 1927 Gulang earthquakes, respectively. The magenta lines in Figure (a) represent the location of the four vertical tomographic profiles named AA', BB', CC' and DD' in Fig. 4.

Discussion

The dominant finding in this paper is that the focal areas of the 1920 Haiyuan and 1927 Gulang earthquakes are both characterized by 3-D high-V anomalies above 15 km, which has also been revealed by former deep seismic sounding and magnetotelluric profiles^{30,33,38}. Besides, the seismogenic faults exactly cut through the high-V bodies (Fig. 4). The high-velocity structures around these two large earthquakes are located around the Precambrian basement and/or Neoproterozoic to Early Paleozoic ophiolite sequences^{40,41}.

Similar high-V anomalies around large earthquakes have been observed by many large earthquakes, such as the 1966 Parkfield M6 earthquake^{14,16}, 1995 southern Hyogo M7.3 earthquake¹⁸, 2004 M6.8 Niigata–Chuetsu earthquake⁴², 2008 Mw7.9 Wenchuan earthquake⁴³, 2010 Ms7.1 Yushu earthquake^{44,45}, 2011 Tohoku-oki Mw 9.0 earthquake⁴⁶, 2013 Ms7.0 Lushan earthquake^{47,48} and 2015 Mw7.8 Gorkha earthquake¹⁵. Therefore, it is probably a universal phenomenon that the high-V bodies in the source regions of large earthquakes represent the asperities in fault planes, which are essential elements for large earthquake generation.

The asperity model^{8,49} has been widely adopted to explain the seismogenic mechanism of main shock of large earthquakes. The term asperity was originally defined as "unevenness of surface, roughness or ruggedness". Smooth surfaces, even those polished to a mirror, are not truly smooth on a microscopic scale. Surface asperities exist across multiple scales, and seismic asperity on a fault plane is at a macroscopic scale. Simply speaking, the asperity is a locked area before an earthquake (Fig. 5a), which has stronger localized mechanical coupling in the source region and is able to offer greater than average resistance to rupture⁸. The asperity will block fault from slipping or the fault slip will destroy the asperity in the fault plane. So the strength of asperity plays an important role in the initiation of fault slip. The stronger the asperity is, the more difficult the fault sliding is. Stress incessantly accumulates on the asperity in the interseismic period due to tectonic loading (Fig. 5b) until fault failure (Fig. 5c), and the maximum slip usually occurs at the asperity zone^{8,50}. Generally, high-V bodies have high density, small porosity and then high strength⁵¹. Therefore, high-V bodies represent asperities and are the fundamental cause for the locking of fault planes, which finally contribute to the generation of large earthquakes.

If the close relationship between the asperity and high-V bodies is valid for most of the large earthquakes, it can be used to predict potential large earthquakes and estimate the seismogenic capability of faults in light of structure studies. In this work, there are clear high-V anomalies above 15 km crossing the Tianjingshan fault (Fig. 3), which suggests strong potential for large earthquakes. We then searched the history earthquakes from Chinese Earthquake Catalog and found the 1709 Zhongwei M7.5 earthquake (latitude 37.4°N, longitude 105.3°E) just occurred there, which validates our conclusion. Therefore, if similar tomographic structure researches are carried out on all active large faults, it will be a great contribution to earthquake prevention and disaster reduction.

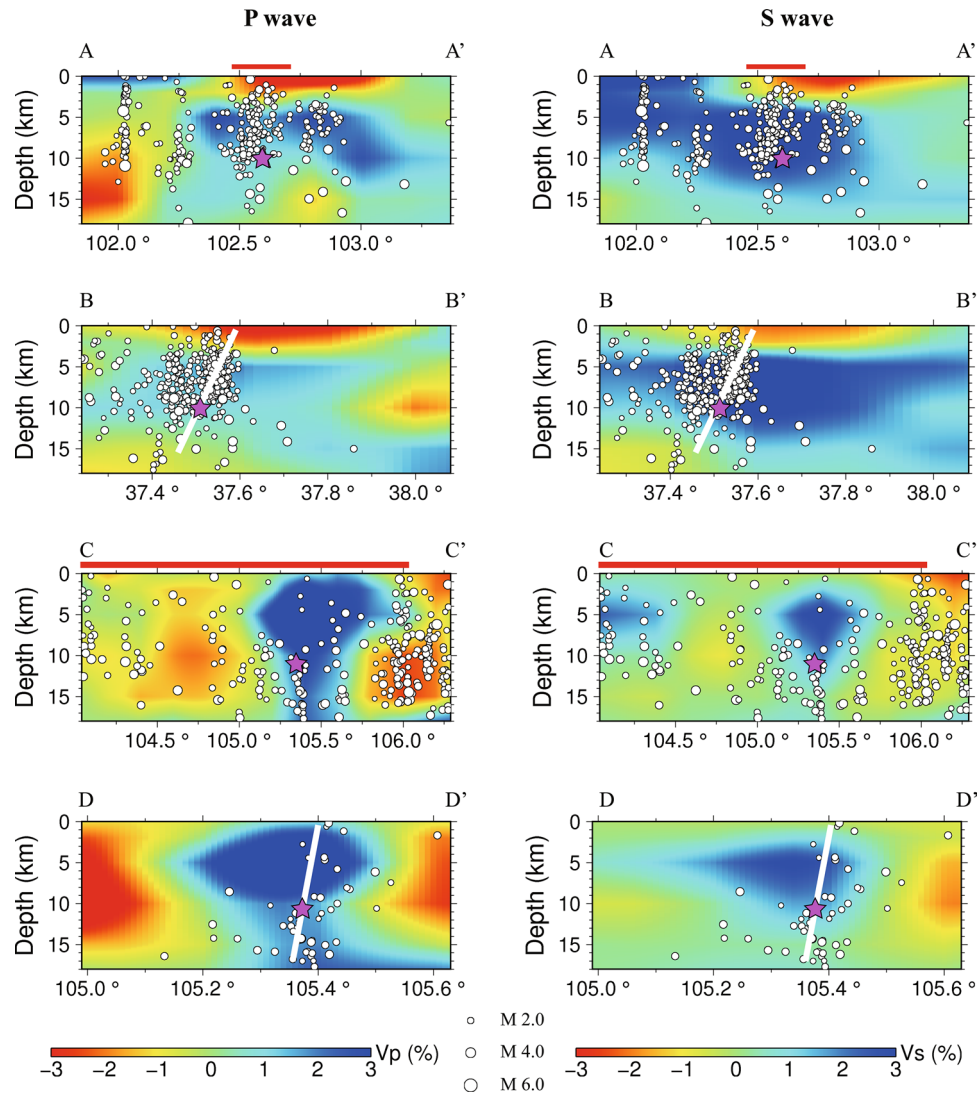


Figure 4. Vertical P and S wave tomographic images with relocated earthquakes. The thick red lines on the profile of AA' and CC' show the rough surface rupture zones of the two large earthquakes, and the white lines represent the major faults.

Methods

The double-difference seismic tomography method (tomoDD)⁵² is developed from the double-difference hypocentral location method (hypoDD)⁵³ and has the advantage to obtain the hypocentral locations and velocity structure simultaneously. TomoDD is suitable for local-scale tomography^{43,54}. There are at least two issues need to be addressed when applied to large study areas for guaranteeing a reliable result. First, tomoDD simply sets the Moho discontinuity as a gradational rather a sharp interface, which inevitably biases the velocity structure around the Moho discontinuity. This problem is especially severe in our study area where the Moho depth contrast can be as large as 30 km between the thick NE Tibetan Plateau and the Ordos and Alxa blocks^{55,56}. Second, tomoDD usually only uses first-arrival phases in the inversion, however there are plenty of later-arrival phases such as Pg and Sg waves in large epicentral distance over 200 km. These phases are essential for improving the coverage and crossing of ray paths in the middle-to-lower crust and thus could better constrain the velocity structure there.

To enhance the tomographic resolution, we improved the tomoDD method mainly in two aspects. First, detailed Moho depths beneath the study area are added as a prior information in the inversion, which help to obtain high-accuracy travel times of first-arrival Pn and Sn phases. The Moho results are mainly obtained from the dense stations of ChinArray⁵⁵. For the areas out the coverage of ChinArray stations, the Moho results are collected from He et al.⁵⁷. Second, we modified the ray tracing of tomoDD method for enabling to calculate the travel times of later-arrival Pg and Sg phases.

We set up a 3-D velocity model with horizontal spacing of 0.2° and ~5 km in depth according to the data density and checkerboard tests. Referring to the detailed 2-D velocity results from active-source seismic profiling in the study region⁵⁸, we constructed the initial velocity model with the Moho depth taken into account (Figure S2).

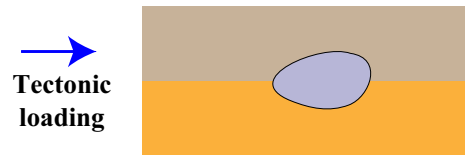
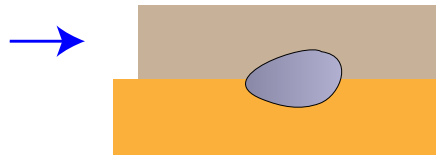
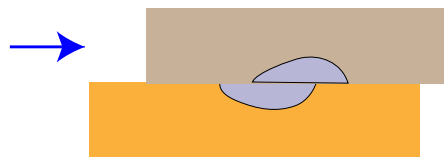
(a) Initial phase**(b) Earthquake preparation****(c) After the earthquake**

Figure 5. The cartoon illustrates the mechanism of preparation and generation of large earthquakes.

The LSQR algorithm⁵⁹ is used to solve the large and sparse system of observation equations which link the observed travel times to the unknown hypocentral and 3-D velocity parameters in tomoDD method. In order to minimize the instability during the inversion and balance model smoothness versus data fitting, smoothing and damping regularizations are adopted in the inversion. After testing different values of smoothing and damping parameters for finding the optimal trade-off point between the RMS of travel-time residual and the norm of the 3-D velocity model, the values of 10 and 600 were selected for the smoothing and damping parameters, respectively.

Received: 1 July 2020; Accepted: 9 February 2021

Published online: 03 March 2021

References

- Lay, T. The surge of great earthquakes from 2004 to 2014. *Earth Planet. Sci. Lett.* **409**, 133–146. <https://doi.org/10.1016/j.epsl.2014.10.047> (2015).
- Harris, R. A. & Day, S. M. Dynamic 3D simulations of earthquakes on En Echelon faults. *Geophys. Res. Lett.* **26**, 2089–2092. <https://doi.org/10.1029/1999gl900377> (1999).
- Wesnowsky, S. G. Displacement and geometrical characteristics of earthquake surface ruptures: Issues and implications for seismic-hazard analysis and the process of earthquake rupture. *Bull. Seismol. Soc. Am.* **98**, 1609–1632. <https://doi.org/10.1785/0120070111> (2008).
- Scognamiglio, L. *et al.* Complex fault geometry and rupture dynamics of the Mw6.5, 30 October 2016, central Italy earthquake. *J. Geophys. Res.: Solid Earth* **123**, 2943–2964. <https://doi.org/10.1002/2018jb015603> (2018).
- Eberhart-Phillips, D. *et al.* The 2002 Denali fault earthquake, Alaska: a large magnitude, slip-partitioned event. *Science* **300**, 1113–1118. <https://doi.org/10.1126/science.1082703> (2003).
- Dragert, H. Mediating plate convergence. *Science* **315**, 471–472. <https://doi.org/10.1126/science.1137171> (2007).
- Lay, T. & Kanamori, H. in *Earthquake Prediction* (eds David W. Simpson & Paul G. Richards) 579–592 (1981).
- Kanamori, H. & Stewart, G. S. Seismological aspects of the Guatemala Earthquake of February 4, 1976. *J. Geophys. Res.: Solid Earth* **83**, 3427–3434. <https://doi.org/10.1029/JB083iB07p03427> (1978).
- Ikari, M. J., Marone, C. & Saffer, D. M. On the relation between fault strength and frictional stability. *Geology* **39**, 83–86. <https://doi.org/10.1130/g31416.1> (2011).
- Hardebeck, J. L. & Loveless, J. P. Creeping subduction zones are weaker than locked subduction zones. *Nat. Geosci.* **11**, 60–64. <https://doi.org/10.1038/s41561-017-0032-1> (2017).
- Scholz, C. H. & Campos, J. On the mechanism of seismic decoupling and back arc spreading at subduction zones. *J. Geophys. Res.: Solid Earth* **100**, 22103–22115. <https://doi.org/10.1029/95jb01869> (1995).
- Chiapparba, C. & Selvaggi, G. Structural control on fault geometry: Example of the Grevena Ms 6.6, normal faulting earthquake. *J. Geophys. Res.: Solid Earth* **102**, 22445–22457. <https://doi.org/10.1029/97jb01385> (1997).
- Lees, J. M. Tomographic P-wave velocity images of the Loma-Prieta earthquake asperity. *Geophys. Res. Lett.* **17**, 1433–1436. <https://doi.org/10.1029/GL017i009p01433> (1990).
- Michael, A. J. & Eberhart-Phillips, D. Relations among fault behavior, subsurface geology, and 3-dimensional velocity models. *Science* **253**, 651–654. <https://doi.org/10.1126/science.253.5020.651> (1991).

15. Pei, S., Liu, H., Bai, L., Liu, Y. & Sun, Q. High-resolution seismic tomography of the 2015 Mw7.8 Gorkha earthquake, Nepal: Evidence for the crustal tearing of the Himalayan rift. *Geophys. Res. Lett.* **43**, 9045–9052. <https://doi.org/10.1002/2016gl069808> (2016).
16. Eberhart-Phillips, D. & Michael, A. J. Three-dimensional velocity structure, seismicity, and fault structure in the Parkfield Region, central California. *J. Geophys. Res.* **98**, 15737. <https://doi.org/10.1029/93jb01029> (1993).
17. Wang, Z., Huang, W., Zhao, D. & Pei, S. Mapping the Tohoku forearc: Implications for the mechanism of the 2011 East Japan earthquake (Mw 9.0). *Tectonophysics* **524–525**, 147–154. <https://doi.org/10.1016/j.tecto.2011.12.032> (2012).
18. Okada, T. *et al.* Imaging the source area of the 1995 southern Hyogo (Kobe) earthquake (M7.3) using double-difference tomography. *Earth Planet. Sci. Lett.* **253**, 143–150. <https://doi.org/10.1016/j.epsl.2006.10.022> (2007).
19. Engelder, T. Aspects of asperity-surface interaction and surface damage of rocks during experimental frictional sliding. *Pure Appl. Geophys.* **116**, 705–716. <https://doi.org/10.1007/BF00876533> (1978).
20. Li, Z., Tian, B., Liu, S. & Yang, J. Asperity of the 2013 Lushan earthquake in the eastern margin of Tibetan Plateau from seismic tomography and aftershock relocation. *Geophys. J. Int.* **195**, 2016–2022. <https://doi.org/10.1093/gji/ggt370> (2013).
21. Sokos, E. *et al.* Asperity break after 12 years: the Mw 6.4 2015 Lefkada (Greece) earthquake. *Geophys. Res. Lett.* **43**, 6137–6145. <https://doi.org/10.1002/2016gl069427> (2016).
22. Kato, N. & Yoshida, S. A shallow strong patch model for the 2011 great Tohoku-oki earthquake: A numerical simulation. *Geophys. Res. Lett.* **38**, L00G04. <https://doi.org/10.1029/2011gl048565> (2011).
23. Hou, K., Deng, Q. & Liu, B. Research on tectonic environment and seismogenic mechanism of 1927 Gulang great earthquake. *Earthq. Res. China* **15**, 339–348 (1999) ((in Chinese)).
24. Motagh, M. *et al.* Coseismic slip model of the 2007 August Pisco earthquake (Peru) as constrained by Wide Swath radar observations. *Geophys. J. Int.* **174**, 842–848. <https://doi.org/10.1111/j.1365-246X.2008.03852.x> (2008).
25. Bilek, S. L. & Engdahl, E. R. Rupture characterization and aftershock relocations for the 1994 and 2006 tsunami earthquakes in the Java subduction zone. *Geophys. Res. Lett.* **34**, doi:<https://doi.org/10.1029/2007gl031357> (2007).
26. Deng, Q. *et al.* Active tectonics and earthquake activities in China. *Earth Sci. Front.* **10**, 66–73 (2003) ((in Chinese)).
27. Wessel, P. & Smith, W. H. F. New, improved version of the generic mapping tools released. *Eos Trans. Am. Geophys. Union* **79**, 579–579 (1998).
28. Zheng, X., Yao, Z., Liang, J. & Zheng, J. The role played and opportunities provided by IGP DMC of China National Seismic Network in Wenchuan earthquake disaster relief and researches. *Bull. Seismol. Soc. Am.* **100**, 2866–2872. <https://doi.org/10.1785/0120090257> (2010).
29. Pei, S. *et al.* Upper mantle seismic velocities and anisotropy in China determined through Pn and Sn tomography. *J. Geophys. Res.* **112**, B05312. <https://doi.org/10.1029/2006jb004409> (2007).
30. Li, S. *et al.* Study on crust structure of Haiyuan strong earthquake region. *Earthq. Res. China* **17**, 16–23 (2001) ((in Chinese)).
31. Burchfiel, B. C. *et al.* Geology of the Haiyuan fault zone, Ningxia-Hui autonomous region, China, and its relation to the evolution of the Northeastern margin of the Tibetan Plateau. *Tectonics* **10**, 1091–1110. <https://doi.org/10.1029/90tc02685> (1991).
32. Zhang, W. Q. *et al.* Displacement along the Haiyuan fault associated with the great 1920 Haiyuan, China, earthquake. *Bull. Seismol. Soc. Am.* **77**, 117–131 (1987).
33. Zhan, Y. *et al.* Crustal electric structure of Haiyuan arcuate tectonic region in the northeastern margin of Qinghai-Xizang Plateau, China. *Acta Seismol. Sin.* **27**, 431–440 (2005) ((in Chinese)).
34. Hou, K. & Wu, Q. Fundamental characteristics of Gulang Ms8 earthquake in 1927. *Earthq. Res. Plateau* **11**, 12–18 (1999) ((in Chinese)).
35. Xu, X., Yeats, R. S. & Yu, G. Five short historical earthquake surface ruptures near the Silk Road, Gansu province, China. *Bull. Seismol. Soc. Am.* **100**, 541–561. <https://doi.org/10.1785/0120080282> (2010).
36. Chen, J., Liu, Q., Li, S., Guo, B. & Lai, Y. Crust and upper mantle S-wave velocity structure across Northeastern Tibetan Plateau and Ordos block. *Chinese J. Geophys.* **48**, 333–342 (2005) ((in Chinese)).
37. Li, H., Xu, X. & Ma, W. Double-difference tomography in Tianzhu-Gulang region and discussion on seismotectonics of 1927 Gulang M.80 earthquake. *Acta Seismol. Sin.* **33**, 156–164 (2011) ((in Chinese)).
38. Zhan, Y. *et al.* Deep electric structure beneath the epicentre of the 1927 Gulang M8 earthquake and its adjacent areas from magnetotelluric sounding, China. *J. Geophys.* **51**, 511–520 (2008) ((in Chinese)).
39. Wang, X., Fang, J. & Xu, H. 3D density structure of lithosphere beneath northeastern margin of the Tibetan Plateau. *Chin. J. Geophys.* **56**, 3770–3778. <https://doi.org/10.6038/cjg20131118> (2013) ((in Chinese)).
40. Song, S., Niu, Y., Su, L. & Xia, X. Tectonics of the North Qilian orogeny, NW China. *Gondwana Res.* **23**, 1378–1401. <https://doi.org/10.1016/j.jr.2012.02.004> (2013).
41. Xu, Y. J. *et al.* Detrital zircon record of continental collision: Assembly of the Qilian Orogen, China. *Sediment. Geol.* **230**, 35–45. <https://doi.org/10.1016/j.sedgeo.2010.06.020> (2010).
42. Okada, T. *et al.* Detailed imaging of the fault planes of the 2004 Niigata-Chuetsu, central Japan, earthquake sequence by double-difference tomography. *Earth Planet. Sci. Lett.* **244**, 32–43. <https://doi.org/10.1016/j.epsl.2006.02.010> (2006).
43. Pei, S. *et al.* Three-dimensional seismic velocity structure across the 2008 Wenchuan Ms 8.0 earthquake, Sichuan. *China. Tectonophysics* **491**, 211–217. <https://doi.org/10.1016/j.tecto.2009.08.039> (2010).
44. evidence from aftershock tomography. Pei, S. & Chen, Y. J. Link between seismic velocity structure and the 2010 Ms 7.1 Yushu earthquake, Qinghai, China. *Bull. Seismol. Soc. Am.* **102**, 445–450. <https://doi.org/10.1785/0120110138> (2012).
45. Pei, S., Chen, Y. J., Feng, B., Gao, X. & Su, J. High-resolution seismic velocity structure and azimuthal anisotropy around the 2010 Ms=7.1 Yushu earthquake, Qinghai, China from 2D tomography. *Tectonophysics* **584**, 144–151. <https://doi.org/10.1016/j.tecto.2012.08.020> (2013).
46. Insight from seismic tomography. Huang, Z. & Zhao, D. Mechanism of the 2011 Tohoku-oki earthquake (Mw 9.0) and tsunamis. *J. Asian Earth Sci.* **70–71**, 160–168. <https://doi.org/10.1016/j.jseaeas.2013.03.010> (2013).
47. Pei, S., Zhang, H., Su, J. & Cui, Z. Ductile gap between the Wenchuan and Lushan earthquakes revealed from the two-dimensional Pg seismic tomography. *Sci. Rep.* **4**, 6489. <https://doi.org/10.1038/srep06489> (2014).
48. Pei, S. *et al.* Seismic velocity reduction and accelerated recovery due to earthquakes on the Longmenshan fault. *Nat. Geosci.* **12**, 387–392. <https://doi.org/10.1038/s41561-019-0347-1> (2019).
49. Aki, K. Asperities, barriers, characteristic earthquakes and strong motion prediction. *J. Geophys. Res.: Solid Earth* **89**, 5867–5872. <https://doi.org/10.1029/JB089iB07p05867> (1984).
50. Lei, X. How do asperities fracture? An experimental study of unbroken asperities. *Earth Planet. Sci. Lett.* **213**, 347–359. [https://doi.org/10.1016/s0012-821x\(03\)00328-5](https://doi.org/10.1016/s0012-821x(03)00328-5) (2003).
51. Tenthorey, E., Cox, S. F. & Todd, H. F. Evolution of strength recovery and permeability during fluid-rock reaction in experimental fault zones. *Earth Planet. Sci. Lett.* **206**, 161–172. [https://doi.org/10.1016/S0012-821x\(02\)01082-8](https://doi.org/10.1016/S0012-821x(02)01082-8) (2003).
52. Zhang, H. & Thurber, C. H. Double-difference tomography: The method and its application to the Hayward Fault, California. *Bull. Seismol. Soc. Am.* **93**, 1875–1889. <https://doi.org/10.1785/0120020190> (2003).
53. Waldhauser, F. & Ellsworth, W. L. A double-difference earthquake location algorithm: Method and application to the northern Hayward fault, California. *Bull. Seismol. Soc. Am.* **90**, 1353–1368. <https://doi.org/10.1785/0120000006> (2000).
54. Zhang, H., Wang, F., Myhill, R. & Guo, H. Slab morphology and deformation beneath Izu-Bonin. *Nat. Commun.* **10**, 1310. <https://doi.org/10.1038/s41467-019-09279-7> (2019).

55. Wang, X. C. *et al.* Three-dimensional lithospheric S wave velocity model of the NE Tibetan Plateau and western North China Craton. *J. Geophys. Res.: Solid Earth* **122**, 6703–6720. <https://doi.org/10.1002/2017jb014203> (2017).
56. Xu, X., Niu, F., Ding, Z. & Chen, Q. Complicated crustal deformation beneath the NE margin of the Tibetan plateau and its adjacent areas revealed by multi-station receiver-function gathering. *Earth Planet. Sci. Lett.* **497**, 204–216. <https://doi.org/10.1016/j.epsl.2018.06.010> (2018).
57. He, R., Shang, X., Yu, C., Zhang, H. & Van der Hilst, R. D. A unified map of Moho depth and Vp/Vs ratio of continental China by receiver function analysis. *Geophys. J. Int.* **199**, 1910–1918. <https://doi.org/10.1093/gji/ggu365> (2014).
58. Zhang, Z. *et al.* Crustal structure across northeastern Tibet from wide-angle seismic profiling: constraints on the Caledonian Qilian orogeny and its reactivation. *Tectonophysics* **606**, 140–159. <https://doi.org/10.1016/j.tecto.2013.02.040> (2013).
59. Paige, C. C. & Saunders, M. A. LSQR: An algorithm for sparse linear equations and sparse least squares. *ACM Trans. Math. Softw.* **8**, 43–71. <https://doi.org/10.1145/355984.355989> (1982).

Acknowledgements

We thank the Center of the China Earthquake Networks (<http://data.earthquake.cn/>) for providing the seismic data in this study. This work was supported by the National Key R&D Program of China (2017YFC1500303), the Strategic Priority Research Program of Chinese Academy of Sciences (XDA20070302) and the National Natural Science Foundation of China (U2039203, 41674090, 41490610).

Author contributions

J.L., L.L. and H.Z. are responsible for collecting the seismic data. Y.L. and X.X. are responsible for processing the data. Q.S. and S.P. improved the method and conducted the inversion. Q.S., S.P., Z.C. and Y.J.C. contributed to interpretation and writing.

Competing interests

The authors declare no competing interests.

Additional information

Supplementary information The online version contains supplementary material available at <https://doi.org/10.1038/s41598-021-84642-7>.

Correspondence and requests for materials should be addressed to S.P.

Reprints and permissions information is available at www.nature.com/reprints.

Publisher's note Springer Nature remains neutral with regard to jurisdictional claims in published maps and institutional affiliations.



Open Access This article is licensed under a Creative Commons Attribution 4.0 International License, which permits use, sharing, adaptation, distribution and reproduction in any medium or format, as long as you give appropriate credit to the original author(s) and the source, provide a link to the Creative Commons licence, and indicate if changes were made. The images or other third party material in this article are included in the article's Creative Commons licence, unless indicated otherwise in a credit line to the material. If material is not included in the article's Creative Commons licence and your intended use is not permitted by statutory regulation or exceeds the permitted use, you will need to obtain permission directly from the copyright holder. To view a copy of this licence, visit <http://creativecommons.org/licenses/by/4.0/>.

© The Author(s) 2021